Estimating zero-plane displacement height and aerodynamic roughness length using synthesis of LiDAR and SPOT-5 data

X. Tian [a,b,*], Z.Y. Li [a], C. van der Tol [b], Z. Su [b], X. Li [c], Q.S. He [d], Y.F. Bao [d,e], E.X. Chen [a], L.H. Li [b]

[a] Research Institute of Forest Resource Information Techniques, Chinese Academy of Forestry, Wanshoushanhou, 100091, Beijing, PR China
[b] Faculty of Geo-Information Science and Earth Observation, University of Twente, Hengelosestraat 99, 7500 AA, Enschede, The Netherlands
[c] Cold and Arid Regions Environmental and Engineering Research Institute, Chinese Academy of Sciences, Donggang West Road 320, 730000, Lanzhou, PR China
[d] Institute of Remote Sensing Applications, Chinese Academy of Sciences, Datun Road, 100101, Beijing, PR China
[e] Beijing Institute of Space Mechanics and Electricity, Zhongguancun Road 99, 100190, Beijing, PR China

ARTICLE INFO

ABSTRACT

In this study, a combination of low and high density airborne LiDAR and satellite SPOT-5 HRG data were used in conjunction with ground measurements of forest structure to parameterize four models for zero-plane displacement height d(m) and aerodynamic roughness length z_{0m}(m), over cool-temperate forests in Heihe River basin, an arid region of Northwest China. For the whole study area, forest structural parameters including tree height (Ht) (m), first branch height (FBH) (m), crown width (CW) (m) and stand density (SD) (trees ha^{-1}) were derived by stepwise multiple linear regressions of ground-based forest measurements and height quantiles and fractional canopy cover (f_c) derived from the low density LiDAR data. The high density LiDAR data, which covered a much smaller area than the low density LiDAR data, were used to relate SPOT-5's reflectance to the effective plant area index (PAIe) of the forest. This was done by linear spectrum decomposition and Li–Strahler geometric–optical models. The result of the SPOT-5 spectrum decomposition was applied to the whole area to calculate PAIe (and leaf area index LAI). Then, four roughness models were applied to the study area with these vegetation data derived from the LiDAR and SPOT-5 as input. For validation, measurements at an eddy covariance site in the study area were used. Finally, the four models were compared by plotting histograms of the accumulative distribution of modeled d and z_{0m} in the study area. The results showed that the model using by frontal area index (FAI) produced best d estimate, and the model using both LAI and FAI generated the best z_{0m}. Furthermore, all models performed much better when the representative tree height was Lorey's mean height instead of using an arithmetic mean.

© 2011 Elsevier Inc. All rights reserved.

1. Introduction

The Monin–Obukhov Similarity (MOS) theory (Foken, 2006; Monin & Obukhov, 1954) has been frequently used in atmospheric models for numerical weather prediction and climate research (Su et al., 2001). Two parameters play a central role in MOS theory, notably the zero-plane displacement d and the roughness height z_{0m} (Garratt, 1994; Yang & Friedl, 2003). These two parameters significantly influence the momentum exchange between the atmosphere and land surface, and yet they are difficult to estimate in practice. Therefore, studies on d and z_{0m} can improve the understanding of the mechanism of momentum transport (Brutsaert, 1999; Koloskov et al., 2007; Krishnan & Kunhikrishnan, 2002).

Many methods exist to estimate d and z_{0m}. These methods can be classified as either experimental or remote sensing based. Experi-

mental methods are based on measurements of the vertical wind profile in and above the canopy. A disadvantage of experimental methods is that the results are only locally valid, and scaling to the grid cell of a climate or land surface model is difficult (Schaudt & Dickinson, 2000). As a consequence, most these models employ general expressions for d and z_{0m} as a function of the vegetation height h, for example $d/h = 2/3$ and $z_{0m}/h = 1/8$ (Garratt, 1994), or use a look-up table based on the land cover types (Dorman & Sellers, 1989; Wieringa, 1986). Neither of these techniques can capture variations of the density of roughness elements. Alternatives that make the inclusion of these variations in density possible are remote sensing based methods. Robust scaling of d and z_{0m} to regional applications using remote sensing data may result in representative values for grid cells in models (Nakai et al., 2008; Su, 2002; Verhoef et al., 1997; Wang et al., 1998; Wieringa, 1993).

In past decades, several models have been developed for d and z_{0m} as functions of (remotely sensed) vegetation physical structural parameters, such as leaf are index (LAI) (Choudhury & Monteith, 1988), frontal area index (FAI) (Raupach, 1994; Schaudt & Dickinson, 2000), stand density (SD) and stem–branch–leaf distributions (Nakai

et al., 2008). Once these parameters and vegetation height can be retrieved from remote sensing data with sufficient accuracy, they can be easily integrated into these models to estimate regional d and z_{0m} values.

Nevertheless, theoretical and practical problems have limited the retrieval of the vegetation parameters from remote sensing data (Braswell et al., 2003; Hu et al., 2004; Olthof & Fraser, 2007). The optical spectrum is insensitive to some of the parameters of interest (for example, vegetation height). To some other parameters it is only sensitive up to a limit above which the signal saturates (for example, LAI). In addition, retrieval techniques usually suffer from ill-posedness, especially in sparsely vegetated areas with the fragmental landscape. Therefore, application of estimating biophysical characteristics from remote sensing should be more reasonable when it is based on physical algorithms, such as Geometric–Optical and Radiative Transfer (GORT) model, rather than direct inference from spectral indices (Hall et al., 1995; Song & Woodcock, 2002).

Airborne laser scanning (ALS) has recently led to a revolution in remote sensing technology for characterizing the canopy structure, due to its ability to measure three-dimensional information (Koukoulas & Blackburn, 2005; Maltamo et al., 2004). The airborne light detection and ranging (LiDAR) sensor provides multiple echoes per laser pulse. It has been applied successfully for measuring and monitoring vegetation structural data across the landscape (Popescu & Wynne, 2004; Reutebuch et al., 2005; Salas et al., 2010).

In this paper we used a combination of forest inventories, airborne LiDAR and a satellite SPOT-5 HRG image as input for four existing models for d and z_{0m}. The four models were validated against d and z_{0m} derived from eddy covariance (EC) and wind profile measurements in a needle forest located in the study area. The four tested models are those of Choudhury and Monteith (1988), Raupach (1994), Schaudt and Dickinson (2000) and Nakai et al. (2008) (hereafter, CM88, RA94, SD00, and NA08 respectively).

First, by means of stepwise multiple linear regression models, low-density airborne LiDAR data was used to derive the forest structural parameters needed to drive the four roughness models. Moreover, for models' requests, the LAI input was calculated based on the experimental adjustment coefficient and the effective plant area index (PAIe) which was derived from the synthesis of high density LiDAR and SPOT-5 HRG data. Second, these parameters were validated against field measurements obtained in the study area. Then, the validities of the four models were compared by using forest structural measurements and forest structural retrievals from remote sensing data respectively. Finally, the four resulting maps (generated with the four models) of d and z_{0m} were used for further statistical analysis.

2. Site observation

In this study we made use of data collected in the framework of the Watershed Allied Telemetry Experimental Research (WATER) carried out in the Heihe River Basin in Northwest China, in 2008 (Li et al., 2009). Heihe River Basin, the second largest inland river basin, is located between 97°24′–102°10′ E and 37°41′–42°42′ N, with an area of about 130,000 km². It consists of three major geomorphic units: the southern Qilian Mountains, the middle Hexi Corridor, and the northern Alxa Highland, and accordingly, the landscapes are various, including glacier, frozen soil, alpine meadow, forest, irrigated crops, riparian ecosystem, and desert (Gobi) (Fig. 1). Aiming to improve the understanding of physical processes of the land surface–atmosphere interaction in arid regions, the WATER project was composed of simultaneous airborne, satellite-borne remote sensing observations and ground-based measurements.

In addition, a network of meteorological stations and EC stations was established in alpine pasture (100°27′ E, 38°02′ N, 3033 m), mountainous forest (100°15′ E, 38°32′ N, 2835 m) and mountain frontal oasis (100°25′ E, 38°51′ N, 1519 m). Each of the EC systems comprised of at least a 3-dimensional sonic anemometer (CSAT-3, Campbell, Inc., USA), a CO₂ and H₂O gas analyzer (LI-7500, LI-COR, Inc., USA), a wind speed sensor (014A and 034B, Met One Instruments, Inc., USA), a temperature and relative humidity probe (HMP45C, Vaisala, Inc., Finland), a heat flux plate (HFP01, Campbell, Inc., USA), a four-component radiometer (CM3 and CG3, Campbell, Inc., USA) and a data logger (CR5000, Campbell, Inc., USA). Measurements of temperature, wind speed, friction velocity were sampled at a rate of 10 Hz and then processed into 30 min average fluxes using EdiRe software. The processing included outlier removal, coordinate rotation, time lag analysis, frequency response calibration, and WPL correction. Only the data of the mountainous forest site were used in this study. The climate at this site is a temperate continental mountainous climate, with cold and dry winters. The annual precipitation of 350 to 495 mm is concentrated in the summer (Zhou et al., 2007). The mountainous landscape is very heterogeneous. The forest, consisting of *Picea crassifolia*, mixed with a small fraction of *Sabina przewalskii* trees, only survives on the shady slopes (between 2500 and 3300 m altitude), while sparse grass inhabits the sunlit slopes.

In June 2008, a campaign with an airborne LiDAR (LiteMapper 5600 system, Riegl LMS-Q560 scanner) and an onboard CCD (DigiCAM-H/22) camera was carried out over the forest hydrology experimental area of WATER project, the Pailugou and Dayekou watersheds (Fig. 2). The flight height was about 800 m above the local topography, and imaging coverage was about 10 km 6 km. With the wavelength of 1550 nm, a pulse of 3.5 ns at 50 kHz, the overall cloud point density about 1.88 hits per square meter (thereafter low density) was acquired from this LiDAR system. In addition, for the purpose of deriving the individual tree structural parameters, repetitive flights were carried out in a small part of overall campaign area. This intensive LiDAR observation produced the point density with 2–7 hits per square meter (thereafter high density).

After the campaign, a scene of SPOT-5 image was acquired on 10th August 2008. Since the beginning of the campaign, an inventory survey on the forest has been carried out at 85 forest plots, including Ht, diameter breast height (DBH), CW, FBH and SD. Tree with a DBH less than 3 cm was not included in the investigation, and PAIe of some forest plots were measured with LAI-2000 (LI-COR, Inc., USA).

To calculate d and z_{0m} at forest site, under neutral conditions ($|z/L| < 0.05$, where L is the Obukhov length), based on eddy covariance measurements: friction velocity (m s⁻¹) at heights z_1 (20 m) and two wind speeds U_1, U_2 (m s⁻¹) at heights z_1 and z_2 (24 m), the following equations were used (Nakai et al., 2008; Rooney, 2001),

$$d = \frac{z_2 \exp(kU_1 / U_*) / \exp(kU_2 / U_*) - z_1}{\exp(kU_1 / U_*) / \exp(kU_2 / U_*) - 1} \tag{1}$$

$$z_{0m} = \frac{z_1 - d}{exp(kU_1 / U_*)} \tag{2}$$

As the airborne LiDAR data and SPOT-5 image were acquired in June and August 2008, respectively, only the EC data under the neutral conditions during these months (June–August) were applied to Eqs. (1) and (2). Moreover, to avoid the effect of the EC tower's shadow, only a few wind speed measurements within a limited range of the wind directions were used (Nakai et al., 2008). As azimuth angle of the sonic anemometer (CSAT-3) is about 75° (clockwise from north), the range was chosen as from 45° (equal to 75°−30°) to 105° (and to 75° + 30°). The representative d and z_{0m} were obtained by averaging the d and z_{0m} calculations from U_1, U_2 and U_* under the neutral conditions within this range.

3. Methodology

3.1. Remote sensing models for estimating d and z_{0m}

Four models were used to calculate d and z_{0m} from forest structural parameters in this study, and Table 1 lists the required input for each
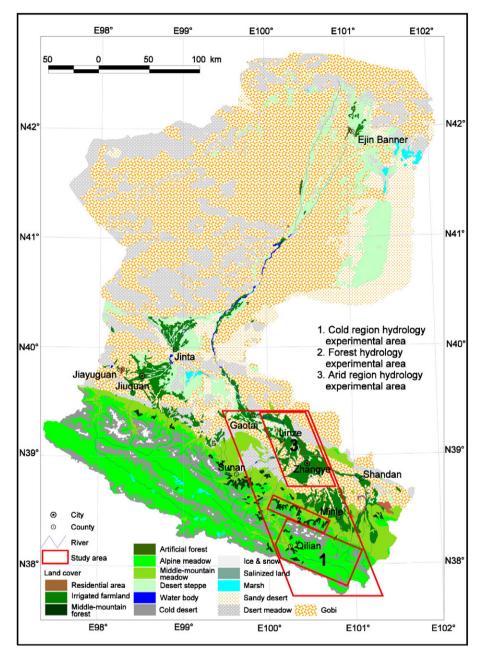
Fig. 1. Heihe River basin and the location of three key experimental areas (the background is the landscape map of the Heihe River basin). Source: (Li et al., 2009).

of the four models. The estimation of the forest structural parameters from LiDAR and SPOT was described in Section 3.3.

The first model is that of Choudhury and Monteith (1988). They used the second-order closure model results of Shaw and Pereira (1982) to estimate d and z_{0m} as follows:

$$d = h\left[ln\left(1 + X^{1/6}\right) + 0.03\, ln\left(1 + X^6\right)\right] \quad (3)$$

$$z_{0m} = \begin{cases} z_{0s} + 0.28hX^{1/2} & \text{for } 0 \leq X \leq 0.2 \\ 0.3h(1-d/h) & \text{for } 0.2 < X \leq 2 \end{cases} \quad (4)$$

where $X = 0.2$LAI, h is the height of the vegetation, and z_{0s} is the soil surface roughness, generally taken as 0.01 m or 0.1 of the height of the vegetation understory, for raw and vegetated substrates respectively (Shuttleworth & Wallace, 1985; Yang & Friedl, 2003).

The second model, Raupach (1994), used observation data to fit the estimation of normalized displacement height d/h and roughness length z_{0m}/h, related to FAI (λ):

$$\frac{d}{h} = 1.0 - \frac{1.0 - \exp(-\sqrt{a_1\lambda})}{\sqrt{a_1\lambda}} \quad (5)$$

$$\frac{z_{0m}}{h} = a_2\exp(-b_2\lambda^{c_2})\lambda^{d_2} + \frac{z_{00}}{h} \quad (\lambda \leq 0.152) \quad (6)$$

$$\frac{z_{0m}}{h} = \frac{a_3}{\lambda^{d_3}}\left[1.0 - \exp(-b_3\lambda^{c_3})\right] + f_2 \quad (\lambda > 0.152) \quad (7)$$

where $a_1 = 15.0$, $a_2 = 5.86$, $b_2 = 10.9$, $c_2 = 1.12$, $d_2 = 1.33$, $a_3 = 0.0537$, $b_3 = 10.9$, $c_3 = 0.874$, $d_3 = 0.510$ and $f_2 = 0.00368$ and $z_{00}/h = 0.00086$.
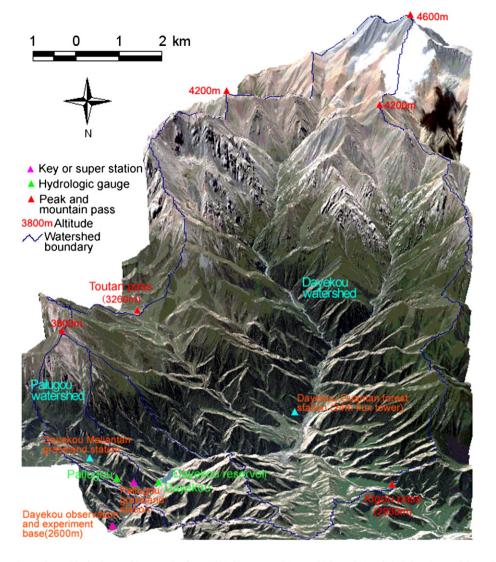
Fig. 2. Forest hydrology experimental area (the background is a mosaic of a Quickbird image overlain on a high resolution digital elevation model, DEM). Source: (Li et al., 2009).

Frontal area index is calculated from the frontal area, A_f, of each individual needle tree as:

$$A_f = h_s {}^* w_s + \frac{1}{2} h_c {}^* w_c \qquad (8)$$

where h_s is the FBH, w_s is DBH, h_c is the height of the crown (i.e. Ht-FBH), w_c is the CW. Then the FAI (λ) is calculated by total A_f divided by the total area of the plot.

Table 1
Required inputs for the four tested roughness models. LAI and Ht are leaf area index and tree height, respectively.

Model	LAI	Ht[a]	CW[a]	FBH[a]	SD[a]
CM88	X	X			
RA94		X	X	X	X
SD00	X	X	X	X	X
NA08	X	X			X

[a] These parameters were used to calculate the frontal area index (FAI) in RA94 and SD00.

In this study, Eq. (8) was further simplified by assuming that the frontal area of the stem is much smaller than the frontal area of the crown (Schaudt & Dickinson, 2000):

$$A_f = \frac{1}{2} h_c {}^* w_c \qquad (9)$$

The third model is that of Schaudt and Dickinson (2000), who estimated z_{0m}/h and d/h over coniferous forest by following expressions:

$$f_z = 0.3299 L_p^{1.5} + 2.1713 \quad \text{for} \quad L_p < 0.8775 \qquad (10)$$

$$f_z = 1.6771 \exp\left(-0.1717 L_p\right) + 1.0 \quad \text{for} \quad L_p \geq 0.8775 \qquad (11)$$

$$L_p = \frac{f_v}{f_c} \text{LAI} - \frac{f_b}{f_c} L_b \qquad (12)$$

$$f_d = 1.0 - 0.3991 \exp\left(-0.1779 L_p\right) \qquad (13)$$

where L_p is the mean plant LAI, L_b is background LAI, f_b is the fraction of the understory vegetation ($f_v = f_c + f_b$). Multiplying f_z to right hand side (RHS) of Eqs. (6) or (7) gives roughness length as a function of

both LAI and FAI. The d/h is quantified by multiplying Eq. (13) by Eq. (5).

The forth model is that of Nakai et al. (2008). They considered the effects of SD, stems/branches and leaves on d/h, based on the following assumptions:

– The fundamental d/h is mainly determined by the SD.
– The seasonal variation depends on the LAI, and the degree of this variation is decided by the SD.
– Total d/h is the collection of above components.

Therefore, the total effect of stems/branches and leaves on d/h was written as follows:

$$\frac{d}{h} = 1.0 - \frac{1.0 - \exp(-\alpha\rho_s)}{\alpha\rho_s} \frac{1.0 - \exp(-\beta A)}{\beta A} \qquad (14)$$

where ρ_s is SD and A is LAI. Nakai et al. (2008) obtained values of the coefficients α and β of $\alpha = 0.000724$ and $\beta = 0.273$ by fitting Eq. (14) to monthly averaged d/h from the EC measurements in their five forest sites. Finally, z_{0m}/h was parameterized by linear regression between d/h and z_{0m}/h as follows:

$$\frac{z_{0m}}{h} = 0.264\left(1.0 - \frac{d}{h}\right) \qquad (15)$$

3.2. Model sensitivity

In order to compare model sensitivities and their dependencies on the roughness elements conditions, a sensitivity analysis for four models was performed. The sensitivity (S_j) of the model to an input parameter (j) can be expressed as:

$$S_j = \frac{Y_j - Y_r}{Y_r} * 100 \qquad (16)$$

where Y_j is the modeling result driven by testing variable j, Y_r is the result predicted by the reference variable r.

The sensitivity tests were conducted for Ht, LAI, FAI and SD variables which directly and significantly affect the d and z_{0m} computations in the four models, as presented in Eqs. (3)–(7) and Eqs. (10)–(16)., The tree measurement at the EC site was used as the reference data r and 0.25*r, 0.75*r, 1.25*r and 1.75*r were used as the testing variables respectively, because this range of values can represent the majority of local roughness element conditions in our study area. The testing variables were then applied to the four models with reference values used for all other inputs to derive the d and z_{0m} values respectively.

As the variations in all model estimates of d and z_{0m} were the same as the prescribed tree height deviations (i.e. d and z_{0m} respond linearly to h in all models), the result of tree height sensitivity was not presented here. The sensitivity results of LAI, FAI and SD are shown in Table 2. In general, the models are more sensitive to variations in tree height than in other parameters, except for FAI in RA94 and SD00: in these models S_j reaches values to $+100\%$ when FAI reduces by -75%. This value exceeds the sensitivity to tree height in both models (-75%). As both RA94 and SD00 used the same expression to derive d and z_{0m} by FAI, they are equally sensitive to FAI. The sensitivity to FAI of the SD00 model also exceeds the sensitivity to LAI. In NA08, SD deviation generated higher discrepancy in both d and z_{0m} estimates than that LAI produced. It is also found that the sensitivity to LAI, FAI and SD, is asymmetric: decreases engender higher S_j than increases. This suggests that at higher values, the response of the models to these variables saturates. The only exception is LAI is for CM88: when LAI is decreased by 75%, then the error ($S_j \sim +15.7\%$) is smaller than when it is increased by 75% ($S \sim -25.5$). This is a particular case, caused by the alternative expression for LAI used for values of LAI smaller than 1 in this model (see Eq. (4)).

The sensitivities of these four models presented here are local sensitivities that somewhat depend on the selection of the reference values. In this study, we have only one EC station in forested area. A more detailed sensitivity analysis with other reference values is not very useful for this study, because the choice of reference values would be rather subjective.

3.3. Forest structural parameters estimated by remote sensing data

The airborne LiDAR data was used to retrieve the f_c, Ht, CW, FBH, SD and PAIe of the forest. Specifically, the PAIe was derived by integration of linear spectrum decomposition model with Li–Strahler's geometric–optical model. In this way, SPOT-5 and LiDAR data were combined, and uncertainties brought about by mixed pixels could be reduced (Section 3.3.2).

3.3.1. LiDAR data process

Both low and high density LiDAR data were processed in this study. The low density LiDAR points were used to extract the digital surface model (DSM) and the digital elevation model (DEM). First, the ground and vegetation points were identified from the overall airborne LiDAR points using Terrasolid software. Then, the DEM with 0.5 m resolution was generated based on the ground points and DSM from the vegetation points. The normalized point (vegetation height) was defined as the height difference between the DSM and the DEM. In order to reduce the influence of the low shrubs, a threshold of 1.3 m was defined to remove normalized points below it in order to refine the vegetation points (He, 2010). The fractional vegetation cover f_c was defined as the complementary of the fraction of laser beam pulses that reached the ground:

$$f_c = 1 - \frac{P}{P_0} \qquad (17)$$

where P_0 is the emitted laser beam and P is the penetrated beam.

Table 2
Sensitivities of the four models with different input parameter variations, as fractions of their reference values.

Parameter models[a]	LAI				FAI				SD			
Deviation	0.25	0.75	1.25	1.75	0.25	0.75	1.25	1.75	0.25	0.75	1.25	1.75
	Sj(%)				Sj(%)				Sj(%)			
CM88-d	−16.3	−3.8	3.8	12.8	–	–	–	–	–	–	–	–
CM88-z₀ₘ	15.7	7.6	−7.6	−25.5	–	–	–	–	–	–	–	–
RA94-d	–	–	–	–	−22.6	−4.0	2.8	6.6	–	–	–	–
RA94-z₀ₘ	–	–	–	–	100	15.8	−10.1	−24.8	–	–	–	–
SD00-d	−16.1	−4.6	3.9	10.2	−22.6	−4.0	2.8	6.6	–	–	–	–
SD00-z₀ₘ	26.8	7.7	−6.6	17.2	100	15.8	−10.1	−24.8	–	–	–	–
NA08-d	−25.2	−7.2	6.2	16.4	–	–	–	–	−28.2	−7.9	6.7	17.5
NA08-z₀ₘ	37.4	10.7	−9.3	−24.3	–	–	–	–	41.8	11.7	−10.0	−26.0

[a] -d and -z₀ₘ are d and z_{0m} models in CM88, RA94, SD00 and NA08, respectively.

The other relevant structural parameters were obtained by regression analysis against field measurements in plots with a size of 20 by 20 m. This spatial resolution was chosen in order to be consistent with the measured plot scale. Stepwise multiple linear regressions between two LiDAR parameters, notably the height quantiles (Lim & Treitz, 2004; Magnussen & Boudewyn, 1998; Næsset, 2004) and f_c, and forest measurements of Ht, CW, FBH, and SD were carried out.

The quantile describes the distribution and location of the sample, expressed as:

$$P\left(X \le \theta_p\right) = p \tag{18}$$

where $P(X \le \theta_p)$ is the cumulative distribution function, X is the population, θ_p is the quantile of population X at p ($0 < p < 1$).

According to their heights, at each plot, the vegetation points were sorted by ascending order, from $p = 5\%$ to $p = 95\%$ (5% interval), resulting in 19 quantiles ($H_{05} \ldots H_{95}$, respectively).

As the stepwise multiple regressions were performed on basis of above 20 statistics (19 quantiles, and f_c, about 75% of measured forest plots (65 out of 85, by stratified sampling)) were used to establish the relationships between above statistics and the forest parameters needed in the four remote sensing roughness models. The optimal regressions were found with SPSS statistical software (see Table 3).

For high density LiDAR data covered area, f_c was also calculated as the ratio of the number of refined vegetation points over the total number of points.

3.3.2. Synthesis of LiDAR and SPOT-5 data

The high resolution DEM from the airborne LiDAR point cloud data was used to geocode the aerial CCD image, thereafter both of them were applied to do the ortho-rectification and topographic correction for the SPOT-5 image. The atmospheric correction for SPOT-5 image was processed with the FLAASH model.

In Li–Strahler model, the average directional reflectance of a pixel can be expressed as a linear combination of the following four components (Li & Strahler, 1985):

$$S = K_{sc}G_{sc} + K_{sb}G_{sb} + K_{dc}G_{dc} + K_{db}G_{db} \tag{19}$$

where S is the mean reflectance from the target surface, G_{sc}, G_{sb}, G_{dc} and G_{db} are the reflected signals of sunlit crown, sunlit background, shadowed canopy and shadowed background, respectively. K's are the areal proportions of the four components. Taking G_0 as the overall reflectance of sc, dc and db and, Eq. (19) can be simplified as:

$$S = K_{sb}G_{sb} + (1 - K_{sb})G_0 \tag{20}$$

and

$$K_{sb} = \exp\left\{-\pi m \left[\sec\theta_i' + \sec\theta_v' - O(\theta_i, \theta_v, \varphi) \right] \right\} \tag{21}$$

Table 3
Stepwise multiple linear regressions for the forest structural parameters used in this study. H_{avg} is the arithmetical average tree height, f_c is the fractional canopy cover and H_{05}, H_{35}, H_{65}, and H_{95} are the height quantiles of 5%, 35%, 65% and 95% respectively.

Forest parameters	Significant statistics	Regression models	Correlation (R^2)
H_{avg}	H_{05}	$Y_{Havg} = 3.525 + 1.025 {*} X_{H05}$	0.70
H_l	H_{90}, H_{35}	$Y_{Hl} = 1.944 + 0.533 {*} X_{H90} + 0.386 {*} X_{H35}$	0.83
FBH	H_{05}	$Y_{FBH} = -0.145 + 0.581 {*} X_{H05}$	0.67
CW	H_{65}, f_c	$Y_{CW} = 1.643 + 0.136 {*} H_{65} + 0.805 {*} f_c$	0.36
SD	H_{95}	$Y_{SD} = 3467.4 - 137.41 {*} X_{H95}$	0.40

where θ_i and θ_v are solar and satellite zenith angle respectively, φ is the azimuth angle between the sun and satellite, $O(\theta_i, \theta_v, \varphi)$ is an 'overlap' function, expressed as:

$$O(\theta_i, \theta_v, \varphi) = (t - \sin t \cos t)\left(\sec\theta_i' + \sec\theta_v'\right) / \pi \tag{22}$$

$$\cos t = \frac{h}{b} \frac{\sqrt{D^2 + \left(\tan\theta_i' \ \tan\theta_v' \ \sin\phi\right)^2}}{\sec\theta_i' + \ \sec\theta_v'} \tag{23}$$

$$D = \sqrt{\tan^2\theta_i' + \tan^2\theta_i' - 2 \ \tan\theta_i' \ \tan\theta_v' \ \cos\phi} \tag{24}$$

$$\tan\theta' = \frac{b}{r} \ \tan\theta \tag{25}$$

where, h is tree height, b and r are major and minor radius of crown.

As the crucial parameter in Eq. (21), the treeness m connects the remote sensing signal and forest structure. It is defined as:

$$m = \rho {*} r_0^2 \tag{26}$$

where ρ is the stand density, r_0 is the average crown width.

Assuming the trees are distributed randomly in the plot, f_c can be also expressed by m (Li & Strahler, 1985),

$$f_c = 1 - e^{-\pi m} \tag{27}$$

According to Monsi and Saeki (2005), the light attenuated by the vegetation canopy is related to vegetation structure and LAI, expressed as,

$$I = I_0 e^{-K {*} LAI} \tag{28}$$

where I and I_0 are light radiation intensities below and above the canopy respectively, k is extinction coefficient. Similarly, for penetrated laser beam of LiDAR, it follows the relation with the emitted laser beam as:

$$P = P_0 e^{-K {*} LAI} \tag{29}$$

Therefore Eq. (17) can be converted into:

$$1 - f_c = e^{-K {*} LAI} \tag{30}$$

As the laser echoes from the leaves were not separated from the overall return points in this study, the derivation was PAIe rather than LAI. Assuming that the leaf inclination angle complies with spherical-shape distribution, k equals to 0.5. Considering that the airborne LiDAR data are taken from the nadir-looking observation, PAIe can be estimated as (Bao, 2009):

$$PAIe \approx -2 \ \ln(1 - fc) = 2\pi m \tag{31}$$

After accurate inversion of f_c from dense LiDAR, parameter m was calculated with Eq. (26). This m was then used together with the geometric data of the SPOT-5 image to calculate K_{sb} with Eqs. (21)–(25). In this way a K_{sb} map for the area of the high density LiDAR campaign was generated. Based on the S samples of the SPOT-5 image selected from this area, and substituting their K_{sb} into the linear spectrum decomposition Eq.(20), the dimidiate end members G_{sb} and G_0 were obtained by factor analysis (Bao, 2009). The values of G_{sb} and G_0 found in this way were applied to the whole low density LiDAR campaign area, including to the part where dense LiDAR data were not collected. Now the values for G_{sb} and G_0 were used in the other direction, first to generate the K_{sb} map for the processed SPOT-5 image
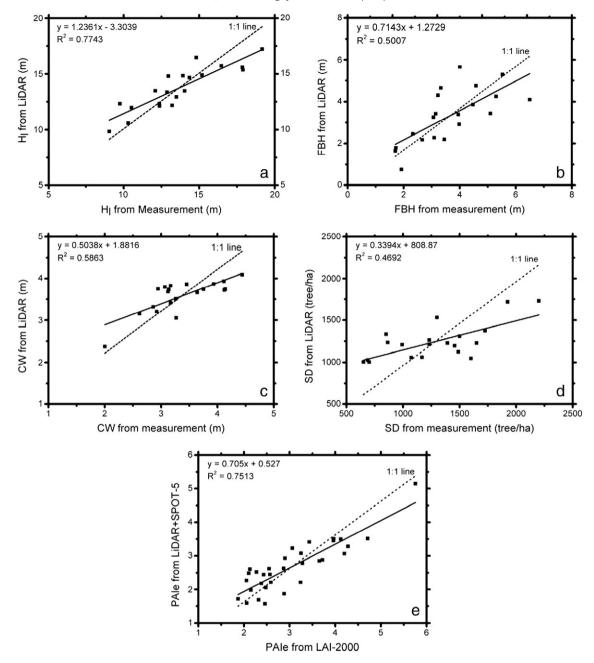
Fig. 3. Validation of H$_l$(a), FBH (b), CW (c), SD (d) and PAle (e) estimates from LiDAR and SPOT-5 data. H$_l$ for Lorey's mean height, FBH for first branch height, CW for crown width, SD for stand density and PAle for effective plant area index.

(Eq. (20)), second to calculate m by inversed Eq. (21) and Eqs. (22)–(25), and finally, to calculate PAle from m with Eq. (31).

As CM88, SD00 and RA08 use LAI as input rather than PAle, the effects of tree trunk, branch and foliage clumping on transforming PAle to LAI should be taken account into. The following formula developed by Chen and Cihlar (1996) was used in this study,

$$LAI = (1-\alpha)*PAle*\gamma_e / \Omega_e \qquad (32)$$

where α is the woody-to-total area ratio, γ_e is the needle-to-shoot area ratio and Ω_e is the element clumping index. In our study area, for *Picea crassifolia*, α, γ_e and Ω_e were found as 0.18, 1.23 and 0.88 respectively (Zou et al., 2009). These values in Eq. (32) result in a ratio
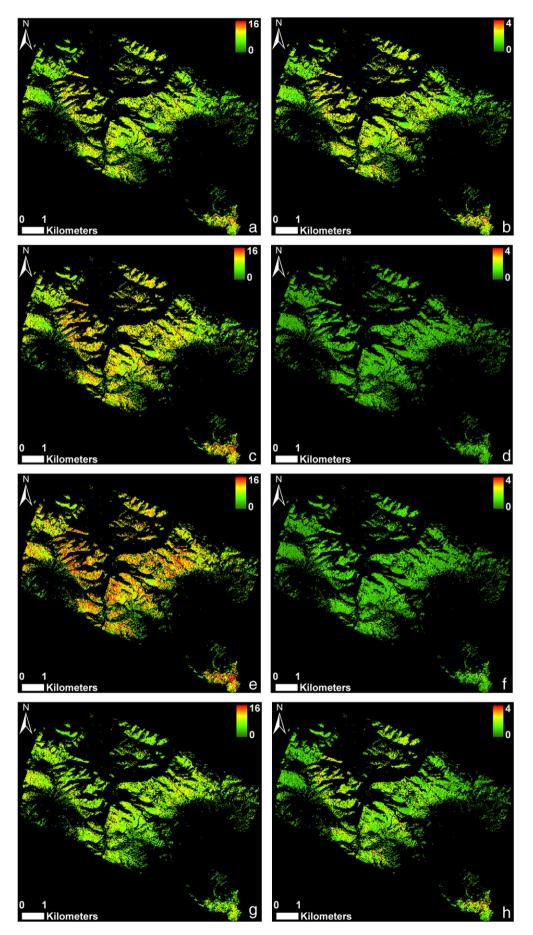
of LAI over PAle of 1.15. One more point to be noted is that, as only a small amount of understory mosses live on the forest floor, and the points below 1.3 m have been separated from vegetation points, the LAI derived from LiDAR and SPOT-5 was also used as a surrogate for L_p in Eqs. (10)–(13).

4. Results

4.1. Forest structural parameters estimated from airborne LiDAR and SPOT-5 data

The variables FBH, CW, SD and Ht (actually the Lorey's mean height (Lorey, 1878), discussed in Section 4.3), were derived at the

Fig. 4. Area-wide d (left) and z_{0m} (right) maps based on CM88 (a and b), RA94 (c and d), SD00 (e and f) and NA08 (g and h) model (unit: meter). CM88, RA94, SD00 and NA08 are the models of Choudhury and Monteith (1988), Raupach (1994), Schaudt and Dickinson (2000) and Nakai et al. (2008), respectively.

plot scale by the relevant height quantiles and f_c from LiDAR vegetation points using regression expressions listed in Table 3. Based on linear decomposition and Li–Strahler models, PAIe and LAI were obtained by use of high density LiDAR could point and SPOT-5 reflectance (Section 3.3.2).

For the Lorey's mean height (H_l), FBH, CW and SD (see Fig. 3(a)–(d)), the stratified selection of 65 forest plots were used for training the regression models and the remaining 20 plots were used for validation. Actually, the original LAI-2000 measurement is PAIe, therefore, instead of LAI, PAIe estimates were validated directly using the measurements at 32 forest plots (see Fig. 3(e)). On the whole, the highest R^2 among the retrievals is about 0.77 for H_l (RMSE~1.35 m), followed by PAIe with R^2~0.75 (RMSE~0.59), and the lowest R^2 is about 0.47 for SD (RMSE~534.52 trees), a little lower than FBH's (R^2~0.50, RMSE~1.03 m) and CW's (R^2~0.59, RMSE~0.68 m).

4.2. d and z_{0m} maps from remote sensing models

Because the tree heights were available, the four maps of d and z_{0m}, corresponding to the four models, were generated (Fig. 4) rather than the fractional maps (d/h's and z_{0m}/h's in some previous studies). As input, H_l and the LiDAR and SPOT-5 retrieved data were used. Overall, the RA94 generated the highest d values with average of 10.61 but lowest z_{0m} values with average of 0.50. On the contrary, NA08 produced the lowest d values with average of 6.82 but highest z_{0m} values with average of 1.57. Both CM88 and SD00 derived the intermediate d and z_{0m} maps with d average of 8.93 and 7.97, and with average z_{0m} of 1.16 and 1.03, respectively. When using the arithmetic mean tree heights instead of H_l, the mean d and z_{0m} values were 6.59 and 0.42, 4.52 and 1.04, 5.91 and 0.77, 4.95 and 0.88, for RA94, NA08, CM88 and SD00, respectively. The overall tendencies and patterns in the maps remained similar, but averaged d and z_{0m} values were lower for all four models than using the H_l.

4.3. Validation and comparison of d and z_{0m} results

The results of the four methods for d and z_{0m} estimates at the EC site are shown in Table 5. As input, the forest inventory data, listed in Table 4 were used. It turns out that for all methods, and both for d and z_{0m}, it is better to use H_l as representative tree height than H_{avg}. Indeed, the representative tree height of the plot would be better expressed by weighting the tree heights of individual trees with the basal areas than taking an arithmetic mean (Nakai et al., 2008). Furthermore, Nakai et al. (2010) proposed that the cumulative basal area inflection (CuBI) height is better index of aerodynamically-determined canopy height than H_l, because H_l would be prone to a small value if there are a large number of low trees. But, the CuBI height seems to be not applicable to some forest plots. For example, in our EC site, only Logistic function and Beta growth function, Eq. (4) and Eq. (10) in Nakai et al. (2010), can fit the plot of the measured cumulative basal area against ascending tree height, and the other four functions are failed to produce the fitting curve. However, the inflection points of these two fitting curves are unrealistically high with 20.38 and 20.71 m respectively, which are higher than the highest tree with 18.50 m.

For these reasons, we used H_l for further analysis in this study:

$$H_l = \frac{\sum_{i=1}^{N} H_i * A_i}{\sum_{i=1}^{N} A_i} \tag{33}$$

where H_i is single tree height, A_i is the tree basal area, N is the total of the trees.

Table 4
Input parameters based on tree measurements.

Forest parameter	Measurement	LiDAR–SPOT-5 estimation
Leaf area index	3.44	3.77
Frontal area index	1.38	1.48
Stand density	1440 (trees ha^{-1})	1265 (trees ha^{-1})
Arithmetical average tree height	9.50 (m)	10.50 (m)
Weighted average tree height	14.52 (m)	14.33 (m)

Table 5 shows that the RA94 produced the highest d but lowest z_{0m} at this site, and NA08 generated the lowest d but highest z_{0m}. The other two models rendered intermediate outcomes for both d and z_{0m}. The RA94 was the closest to the EC measurement of d, but underestimated z_{0m}, whereas the SD00 was the closest to the EC measurement of z_{0m}, but underestimated d.

In analogy to Table 5, Table 6 shows d and z_{0m} for the EC site, now using retrievals from LiDAR and SPOT-5 data as input. It should be noted that the site geographic boundary contains some sub-pixels of remote sensing estimates. Therefore, inside the site boundary, a zonal statistic analysis was performed to extract the average values of input parameters needed in the d and z_{0m} models. Comparing Tables 5 and 6 shows that the values for d and z_{0m} derived with the two input data sets are similar. It did not make a difference whether the LiDAR and SPOT-5 or the field measurements were used as input for the four models. After all, the remote sensing retrievals matched the measurements well (see Table 4). The differences among the four models are higher than the differences caused by the input data.

For further analysis, under the condition of only one validation point (the EC station), the histogram and accumulative probability of the relative difference might be the integrative illustration for the mutual area-wide maps' comparison. Although SD00 largely underestimated the d, it reproduced the EC measurement of z_{0m} well. Considering that most land surface models are more sensitive to z_{0m} than to d, we used d and z_{0m} values from SD00 as the references to calculate the relative difference and to cross-compare the models,

$$S_{rd} = \frac{|S_v - S_{SD00}|}{S_{SD00}} \tag{34}$$

where S_{rd} is the relative difference of d or z_{0m}, S_{SD00} is the SD00 modeled d or z_{0m} and S_v is the derived d or z_{0m} from the other three models.

Then, the d and z_{0m} values of each pixel in the maps of SD00 and other three models were used to generate the d and z_{0m} relative difference maps by Eq. (34). The statistical information of these relative difference maps is shown by their histograms and accumulative probability density curves (see Fig. 5). By analysis of these information, as a whole, for CM88, the relative difference of d (dr$_d$) is moderate with mean ($\bar{u}$) = 0.13, standard deviation (σ) = 0.08, but the relative difference of z_{0m} (dr$_{z0m}$)($\bar{u}$ = 0.17 and σ = 1.08) is the lowest among them. Contrarily, NA08's dr$_d$ ($\bar{u}$ = 0.14, σ = 0.09) is the lowest but the dr$_{z0m}$ ($\bar{u}$ = 0.50, σ = 0.21) is similar to dr$_{z0m}$ ($\bar{u}$ = 0.51, σ = 0.06) of RA94 which generated the highest dr$_{z0m}$ ($\bar{u}$ = 0.34, σ = 0.09). The accumulative probability density functions of the differences dr$_d$ and dr$_{z0m}$, showed that 95% of the area had values of dr$_d$ and dr$_{z0m}$ below 26% and 36% for CM88, below 48% and 57% for RA94, and below 31% and 77% for NA08.

5. Discussion

In this study the statistics of the cloud point of LiDAR measurements were used to retrieve the vertical structure of the canopy. A more accurate alternative is to use high density airborne LiDAR cloud points or full wave form LiDAR observations. In this way sufficient information on individual trees could be derived. The disadvantage of

Table 5
Comparison of d and z_{0m} from remote sensing models using the site measurements as inputs with the EC measurements (unit: meter).

Method	d with H_l	d with H_l	z_{0m} with H_{avg}	z_{0m} with H_l
CM88	6.32	9.66	0.95	1.46
RA94	7.43	11.36	0.44	0.67
SD00	5.82	8.90	0.84	1.28
NA08	5.67	8.67	1.01	1.54
EC	12.60		1.05	

Table 6
Comparison of d and z_{0m} from remote sensing models using LiDAR and SPOT-5 estimates as inputs with the EC measurements (unit: meter).

Method	d with H_{avg}	d with H_l	z_{0m} with H_{avg}	z_{0m} with H_l
CM88	7.09	9.67	1.02	1.40
RA94	8.29	11.32	0.46	0.63
SD00	6.60	9.00	0.87	1.19
NA08	6.21	8.58	1.13	1.57
EC	12.60		1.05	

this approach is that a single flight is insufficient: more overpasses are needed.

As the remote sensing d and z_{0m} models concerned, the LAI based model, CM88, was originally designed for agriculture, thus it might be more applicable in low vegetation area than in high canopy cover. For herbaceous plant or crop, CM88 could represent the roughness element density by LAI, but, for forest, there is no clear relationship between roughness element density (here refers to SD) and LAI. However, according to CM88, z_{0m}/h will monotonically decrease with increasing LAI. It has been well recognized that z_{0m} widely varies (Garratt, 1994; Shaw & Pereira, 1982). It would decline when the canopy aggregates and the high foliage density opposes a resistance to the airflow, as the airflow exerts drag only near the top of the canopy. Conversely, when the canopy becomes sparser, the drag would reduce again. Therefore, z_{0m} should peak at some intermediate value of the roughness element density (Schaudt & Dickinson, 2000). Schaudt and Dickinson (2000) illustrated this kind of z_{0m} variation with LAI and f_c in forest area and Zhou et al. (2006) also figured out it in both experimental agriculture and forest sites.

For RA94, there is also the analogous problem to express the roughness element density by FAI. The experiments of Raupach (1994) were mainly carried out on dense vegetation or solid blocks, and might
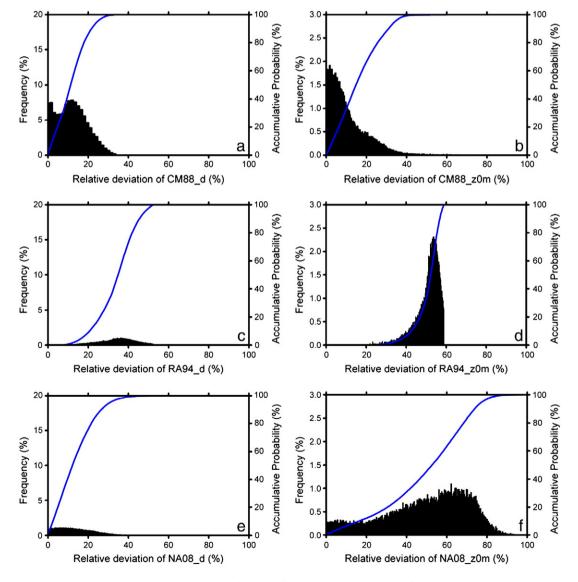

Fig. 5. Histograms (black column) and accumulative probability (blue line) of relative difference of d (left) and z_{0m} (right) from CM88 (a and b), RA94 (c and d) and NA08 (e and f) on basis of SD00 estimates.

not be well suited for sparse roughness element (Schaudt & Dickinson, 2000). For uniformly distributed forest with homogeneous canopy shape, FAI might be proportional to the tree density. Due to the complexity of the canopy shapes and overlaps of the crowns, it is hard to determine the relationship between FAI and the density. Moreover, the site dependent coefficients (i.e. a_1–a_3, b_2, b_3, c_2, c_3, d_2, and d_3 in RA94) might be suitable at the specific patches, but probably be invalid at elsewhere.

A generally applicable model would probably consider more factors affecting the d and z_{0m}, such as limiting infinite LAI by FAI (as in SD00), and inter-site difference presented by SD and seasonal variations depicted by LAI (as in NA08). As NA08's z_{0m} expression was established by linear fitting the observed d/h against z_{0m}/h, the site calibrated coefficient might be not appropriate to our site. SD00 also involves site dependent coefficients, as it was developed on basis of RA94. Although, the SD00 produced the most close z_{0m} to the EC observation, but it underestimate the d to a large extent as well. It might be explained by that, as the EC tower is surrounded by mountains which are close to (about several hundred meters) and higher than the tower, the winds could be elevated by them.

We stress that, although DSM and DEM from LiDAR were used to retrieve the height quantiles, the effect of topography on d and z_{0m} was not taken into account in this study. For the models using FAI (RA94 and SD00), the computation of FAI should consider the variation of the elevation. Moreover, the shape of frontal surface perpendicular to the airflow depends on the wind direction and then FAI will fairly vary. To analyze the topographic and wind directional effects, the footprint of the EC tower should be determined firstly. For this purpose, high density LiDAR data covering the EC tower could be used, as this can provide precise individual tree structural information. The local landscape and topography is very complex, and therefore, a careful analysis of high density LiDAR data would be required. This is beyond the scope of this study. It could also be of interests if the performances of geometrical models (i.e. RA94 and SD00) and those of computational fluid dynamics models are cross-compared.

Generally, a better model performance at the site scale does not mean a wider applicability. For regional retrieval the crucial point is whether the model inputs can be retrieved with sufficient accuracy from remote sensing. Once the robust relevant vegetation structural parameters can be derived by remote sensing method, such as applying POLInSAR techniques for satellite SAR data, analyzing point cloud or waveform data from satellite vegetation canopy LiDAR, these kinds of remote sensing d and z_{0m} models can be practically applied at regional scale. In advance to that, this paper explored to take the advantages of LiDAR point cloud in providing precise three-dimensional information and SPOT-5 imagery in high spatial resolution and multi-spectral information to derive the area-wide d and z_{0m} maps.

Besides the bio-spatial maps including H_l, FBH, CW, SD and LAI retrievals needed by the land surface model, maps of d and z_{0m} can improve eco-hydrological process simulation for the local watersheds. In our study area, eco-hydrological processes in Dayekou and Pailugou watersheds are much critical for the following reaches supported by upper snow-melting water resource. Moreover, these high resolution thematic maps are directly applicable for the d and z_{0m} up-scaling study. These in turn are very important for estimating the regional heat transfer when the medium resolution satellite data (i.e. Landsat TM, ASTER, and MODIS) are applied by remote sensing energy balance models such as SEBS (Su, 2002).

6. Conclusion

This study was the first to apply airborne LiDAR point cloud data and satellite SPOT-5 image to estimate the d and z_{0m}. Based on four models (CM88, RA94, SD00, and NA08), the generated area-wide d and z_{0m} maps are more applicable than the normalized d/h and z_{0m}/h

maps which were normally retrieved from satellite remote sensing data with absence of roughness element height information.

At the forest site, using the inventoried forest structural data, it was tested by EC measurements that, using H_l, all models performed much better than using the average tree height. Using preventative roughness height, among all the model's performances, SD00 outperformed the others in estimating z_{0m}, but it estimated d much lower, and RA94 performed most closely to the measurement in retrieving d, but it rendered the lowest outcome of z_{0m}. The lowest d but largest z_{0m} estimates came from the NA08. CM88 it produced intermediate values of d and z_{0m}.

Reasonable H_l ($R^2 \sim 0.77$), FBH ($R^2 \sim 0.50$), CW ($R^2 \sim 0.59$) and SD ($R^2 \sim 0.47$) estimates were derived by the regression models related to the height quantiles and f_c from low density LiDAR point cloud data. Taking the effects of tree trunk, branch and leaf cluster into account, LAI is calculated by multiplying experimental adjustment coefficient (1.15) and inversed PAIe ($R^2 \sim 0.75$) from synthesis of high density LiDAR (small area) and SPOT-5 data (large area) based on linear spectrum decomposition and Li–Strahler models. Subsequently, using these retrievals, the four remote sensing d and z_{0m} models were applied to retrieve the area-wide d and z_{0m} maps. During this process, the tendency of each model behavior coincided to its former performance driven by forest measurements at the site.

For the comparisons of their entire maps, histograms of relative deviation, using the SD00 as a reference, were analyzed by their statistics information and accumulative probability distributions. On the whole, the variances of other three models compared with the SD00 maps complied with the tendencies as those from site comparisons carried out by both measurement and remote sensing derived results.

Acknowledgement

References

Bao, Y.F. (2009). Study on methods of forest parameters extraction from multi-source remote sensing data. PhD thesis (in Chinese)-Institute of Remote Sensing Applications, Chinese Academy of Sciences, Beijing, China, pp73 – 74.

Braswell, B. H., Hagen, S. C., Frolking, S. E., & Salas, W. A. (2003). A multivariable approach for mapping sub-pixel land cover distributions using MISR and MODIS: Application in the Brazilian Amazon region. Remote Sensing of Environment, 87 (2–3), 243–256.

Brutsaert, W. (1999). Aspects of bulk atmospheric boundary layer similarity under free convective conditions. Reviews of Geophysics, 37(4), 439–451.

Chen, J. M., & Cihlar, J. (1996). Retrieving leaf area index of boreal conifer forests using Landsat TM Images. Remote Sensing of Environment, 55(2), 153–162.

Choudhury, B. J., & Monteith, J. L. (1988). A four-layer model for the heat budget of homogeneous land surfaces. The Quarterly Journal of the Royal Meteorological Society, 114(480), 373–398.

Dorman, J. L., & Sellers, P. J. (1989). A global climatology of albedo, roughness length and stomatal resistance for atmospheric general circulation models as represented by the Simple Biosphere model (SiB). Journal of Applied Meteorology, 28(9), 833–855.

Foken, T. (2006). 50 years of the Monin–Obukhov similarity theory. Boundary Layer Meteorology, 119(3), 431–447.

Garratt, J. R. (1994). The atmospheric boundary layer. Cambridge, New York: Cambridge University Press 316 pp.

Hall, F. G., Shimabukuro, Y., & Huemmrich, K. F. (1995). Remote sensing of forest bio-physical structure using mixture decomposition and geometric reflectance models. *Ecological Applications*, 5(4), 993–1013.

He, Q.S. (2010). Study on forest biomass synergy inversion from multi-source remote sensing data. PhD thesis (in Chinese)-Institute of Remote Sensing Applications, Chinese Academy of Sciences, Beijing, China, pp 69.

Hu, B., Miller, J. R., Chen, J. M., & Hollinger, A. (2004). Retrieval of the canopy leaf area index in the BOREAS flux tower sites using linear spectral mixture analysis. *Remote Sensing of Environment*, 89(2), 176–188.

Koloskov, G., Mukhamejanov, K., & Tanton, T. W. (2007). Monin–Obukhov length as a cornerstone of the SEBAL calculations of evapotranspiration. *Journal of Hydrology*, 335(1–2), 170–179.

Koukoulas, S., & Blackburn, G. A. (2005). Mapping individual tree location, height and species in broadleaved deciduous forest using airborne LiDAR and multi-spectral remotely sensed data. *International Journal of Remote Sensing*, 26(3), 431–455.

Krishnan, P., & Kunhikrishnan, P. K. (2002). Some characteristics of atmospheric surface layer over tropical inland region during southwest monsoon period. *Atmospheric Research*, 62(1–2), 111–124.

Li, X., Li, X. W., Li, Z. Y., Ma, M. G., Wang, J., Xiao, Q., et al. (2009). Watershed allied telemetry experimental research. *Journal of Geophysical Research*, 114(D22103). doi:10.1029/2008JD 011590.

Li, X. W., & Strahler, A. H. (1985). Geometric–optical modeling of a conifer forest canopy. *IEEE Transactions on Geoscience and Remote Sensing*, GE-23(5), 705–721.

Lim, K. S., & Treitz, P. M. (2004). Estimation of above ground forest biomass from airborne discrete return laser scanner data using canopy-based quantile estimators. *Scandinavian Journal of Forest Research*, 19(6), 558–570.

Lorey, T. (1878). Die mittlere Bestandeshohe. *Allg. Forst- u. J. - Ztg.*, 54, 149–155.

Magnussen, S., & Boudewyn, P. (1998). Derivations of stand heights from airborne laser scanner data with canopy-based quantile estimators. *Canadian Journal of Forest Research*, 28(7), 1016–1031.

Maltamo, M., Eerikäinen, K., Pitkänen, J., Hyyppä, J., & Vehmas, M. (2004). Estimation of timber volume and stem density based on scanning laser altimetry and expected tree size distribution functions. *Remote Sensing of Environment*, 90(3), 319–330.

Monin, A. S., & Obukhov, A. M. (1954). Basic laws of turbulent mixing in the ground layer of the atmosphere. *Trudy Geofizicheskogo Instituta, Akademiya Nauk SSSR*, 24 (151), 163–187.

Monsi, M., & Saeki, T. (2005). On the factor light in plant communities and its importance for matter production. *Annals of Botany*, 95(3), 549–567.

Næsset, E. (2004). Practical large-scale forest stand inventory using a small-footprint airborne scanning laser. *Scandinavian Journal of Forest Research*, 19(2), 164–179.

Nakai, T., Sumida, A., Daikoku, K., Matsumoto, K., van der Molen, M. K., Kodama, Y., et al. (2008). Parameterisation of aerodynamic roughness over boreal, cool- and warm-temperate forests. *Agricultural and Forest Meteorology*, 148(12), 1916–1925.

Nakai, T., Sumida, A., Kodama, Y., Hara, T., & Ohta, T. (2010). A comparison between various definitions of forest stand height and aerodynamic canopy height. *Agricultural and Forest Meteorology*, 150(9), 1225–1233.

Olthof, I., & Fraser, R. H. (2007). Mapping northern land cover fractions using Landsat ETM+. *Remote Sensing of Environment*, 107(3), 496–509.

Popescu, S. C., & Wynne, R. H. (2004). Seeing the trees in the forest: Using lidar and multispectral data fusion with local filtering and variable window size for estimating tree height. *Photogrammetric Engineering and Remote Sensing*, 70(5), 589–604.

Raupach, M. R. (1994). Simplified expressions for vegetation roughness length and zero-plane displacement as a function of canopy height and area index. *Boundary-Layer Meteorology*, 71(1–2), 211–216.

Reutebuch, S. E., Andersen, H. E., & McGaughey, R. J. (2005). Light detection and ranging (LIDAR): An emerging tool for multiple resource inventory. *Journal of Forestry*, 103 (6), 286–292.

Rooney, G. G. (2001). Comparison of upwind land use and roughness length measured in the urban boundary layer. *Boundary-Layer Meteorology*, 100(3), 469–486.

Salas, C., Ene, L., Gregoire, T. G., Næsset, E., & Gobakken, T. (2010). Modelling tree diameter from airborne laser scanning derived variables: A comparison of spatial statistical models. *Remote Sensing of Environment*, 114(6), 1277–1285.

Schaudt, K. J., & Dickinson, R. E. (2000). An approach to deriving roughness length and zero-plane displacement height from satellite data, prototyped with BOREAS data. *Agricultural and Forest Meteorology*, 104(2), 143–155.

Shaw, R., & Pereira, A. (1982). Aerodynamic roughness of a plant canopy: A numerical experiment. *Agricultural Meteorology*, 26(1), 51–65.

Shuttleworth, W., & Wallace, J. (1985). Evaporation from sparse crops — An energy combination theory. *The Quarterly Journal of the Royal Meteorological Society*, 111 (469), 839–855.

Song, C., & Woodcock, C. E. (2002). The spatial manifestation of forest succession in optical imagery: The potential of multiresolution imagery. *Remote Sensing of Environment*, 82(2–3), 271–284.

Su, Z. (2002). The Surface Energy Balance System (SEBS) for estimation of turbulent heat fluxes. *Hydrology and Earth System Sciences*, 6(1), 85–99.

Su, Z., Schmugge, T., Kustas, W. P., & Massman, W. J. (2001). An evaluation of two models for estimation of the roughness height for heat transfer between the land surface and the atmosphere. *Journal of Applied Meteorology*, 40(11), 1933–1951.

Verhoef, A., McNaughton, K. G., & Jacobs, A. F. G. (1997). A parameterization of momentum roughness length and displacement height for a wide range of canopy densities. *Hydrology and Earth System Sciences*, 1, 81–91.

Wang, J. M., Bastiaanssen, W. G. M., Ma, Y., & Pelgrum, H. (1998). Aggregation of land surface parameters in the oasis–desert systems of Northwest China. *Hydrological Processes*, 12(13–14), 2133–2147.

Wieringa, J. (1986). Roughness-dependent geographical interpolation of surface wind speed averages. *Quarterly Journal of the Royal Meteorological Society*, 112(473), 867–889.

Wieringa, J. (1993). Representative roughness parameters for homogeneous terrain. *Boundary- Layer Meteorology*, 63(4), 323–363.

Yang, R., & Friedl, M. A. (2003). Determination of roughness lengths for heat and momentum over boreal forests. *Boundary-Layer Meteorology*, 107(3), 581–603.

Zhou, Y. L., Sun, X. M., Zhu, Z. L., Zhang, R. H., Tian, J., Liu, Y. F., et al. (2006). Surface roughness length dynamic over several different surfaces and its effects on modeling fluxes. *Science In China Series D-Earth Sciences*, 49(Supp.2), 262–272.

Zhou, Y., Zhu, Q., Chen, J. M., Wang, Y. Q., Liu, J., Sun, R., et al. (2007). Observation and simulation of net primary productivity in Qilian Mountain, western China. *Journal of Environmental Management*, 85(3), 574–584.

Zou, J., Yan, G. J., Zhu, L., & Zhang, W. M. (2009). Woody-to-total area ratio determination with a multispectral canopy imager. *Tree Physiology*, 29(8), 1069–1080.